A theoretical kinetic study of ĊH3 + #H2: From electronic structure to NH3/CH4 combustion modelling implications

Combustion and Flame 277 (2025) 114232

Contents lists available at ScienceDirect

Combustion and Flame

journal homepage: www.sciencedirect.com/journal/combustion-and-flame

A theoretical kinetic study of $\dot{C}H_3 + \dot{N}H_2$: From electronic structure to NH_3/CH_4 combustion modelling implications

Yuxiang Zhu [a], Stephen J. Klippenstein [b], Henry J. Curran [a], Chong-Wen Zhou [a,*]

[a] Combustion Chemistry Centre, School of Biological and Chemical Sciences, MaREI, Ryan Institute, University of Galway, Galway H91 TK33, Ireland
[b] Chemical Sciences and Engineering Division, Argonne National Laboratory, Lemont, IL 60439, United States

ARTICLE INFO

Keywords:
Ab initio
Theoretical kinetics
Ammonia/methane mixtures
Carbon-nitrogen interactions

ABSTRACT

Carbon–nitrogen interaction reactions play an important role in governing the reactivity of ammonia blended fuels. However, there remains uncertainties regarding their detailed reaction pathways and rate constants, hampering the development of high-fidelity chemical kinetic models. In this study, the kinetics of $\dot{C}H_3 + \dot{N}H_2$, a key C–N interaction reaction in ammonia/methane blend combustion have been investigated. The potential energy surface has been explored using the high-level ANL0F method, yielding highly accurate stationary point energies that agree with ATcT values within 0.1 kcal mol^{-1}. Variable reaction coordinate transition state theory is used to treat the barrierless association and decomposition reaction channels, based on directly sampled radical-radical interaction energies at the CASPT2-F12(2e,2o)/cc-pVTZ-F12 level of theory. The minimum transitional mode numbers of states obtained are then coupled with the RRKM/master equation to calculate temperature- and pressure-dependent rate constants. Our a priori calculations capture available experimental measurements from the literature very well. The calculated rate constants have been incorporated into an NH_3/CH_4 chemical kinetic model currently under development at the University of Galway. The effect of the updated kinetic data for $\dot{C}H_3 + \dot{N}H_2$ on model predicted NH_3/CH_4 fuel reactivity is elucidated.

1. Introduction

Ammonia (NH_3) is a promising alternative to petroleum-based fuels, which can be applied to heavy-duty gas turbines and maritime internal combustion engines [1,2], reducing carbon dioxide (CO_2) emissions, thereby alleviating 'carbon burden' on the atmosphere. One possible option of using NH_3 in engines is co-firing it with natural gas (NG) and/or methane (CH_4) [2,3]. To facilitate its practical application, and address technical issues such as combustion instability with large NH_3 blending portions [2,4] and locate optimal operation conditions, we need to fully understand the combustion chemistry of ammonia/methane blends at engine-relevant conditions.

Blending NH_3 with hydrocarbons leads to potential carbon-nitrogen (C–N) interaction reactions. These play an important role in governing both fuel reactivity and the 'Thermal DeNO$_x$' process of NH_3/hydrocarbon blends [5]. Uncertainties in this chemistry and their corresponding kinetic data limit chemical kinetic model predictions. In the combustion of NH_3/CH_4 mixtures, a considerable portion of CH_4 undergoes H-atom abstraction by amino ($\dot{N}H_2$) radicals, which are abundant in the radical pool produced from NH_3 oxidation. These abstractions form methyl ($\dot{C}H_3$) radicals, which can further react with $\dot{N}H_2$, forming methylamine (CH_3NH_2) and other bimolecular products. The possible reaction channels are as follows:

$$\dot{C}H_3 + \dot{N}H_2 \rightleftharpoons CH_3NH_2 \quad (R1)$$

$$\rightleftharpoons \dot{C}H_2NH_2 + \dot{H} \quad (R2)$$

$$\rightleftharpoons CH_3\dot{N}H + \dot{H} \quad (R3)$$

$$\rightleftharpoons CH_4 + {}^3NH \quad (R4)$$

$$\rightleftharpoons {}^3CH_2 + NH_3 \quad (R5)$$

$$\rightleftharpoons {}^1CHNH_2 + H_2 \quad (R6)$$

$$\rightleftharpoons CH_2NH + H_2 \quad (R7)$$

Recent experimental and kinetic modeling studies [5–8] have highlighted the reaction $\dot{C}H_3 + \dot{N}H_2 \rightleftharpoons CH_3NH_2$ (R1) as being the most reactivity-inhibiting C–N interaction reaction for NH_3/CH_4 mixture ignition delay times (IDTs) in the temperature range of 950–1100 K and at pressures in the range of 20–60 bar. However, available kinetic data

* Corresponding author.
E-mail address: chongwen.zhou@universityofgalway.ie (C.-W. Zhou).

https://doi.org/10.1016/j.combustflame.2025.114232
Received 15 December 2024; Received in revised form 7 May 2025; Accepted 9 May 2025
Available online 22 May 2025

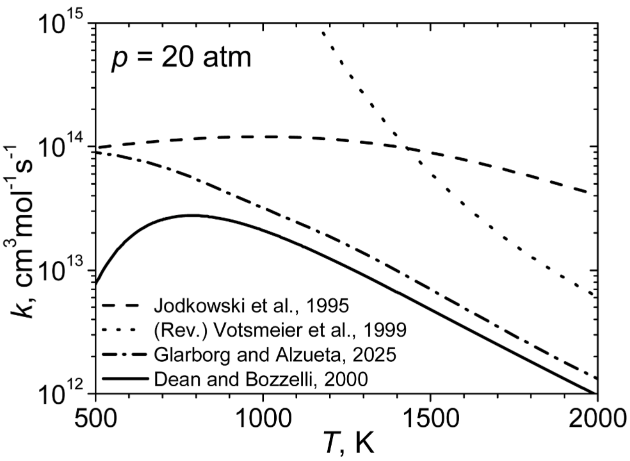

Fig. 1. Available rate constant expressions [9–12] for $\dot{C}H_3 + \dot{N}H_2 \rightleftharpoons CH_3NH_2$ (R1) used in different chemical kinetic models [5,6,8,13–15].

for $\dot{C}H_3 + \dot{N}H_2$ remain limited and show significant deviation [9–12]. Fig. 1 illustrates the rate constants for R1 at 20 atm used in different models [5,6,8,12–15]. Dean and Bozzelli [9] estimated the pressure-dependent rate constant for R1–R3 and R7 using the QRRK/MSC method and provided rate constant expressions at 0.1, 1, and 10 atm. Their rate constant results in an under-estimation of mixture reactivity when applied to pressures above 10 atm. Rate constants for R4 and R5 estimated using the 'direct hydrogen transfer (DHT)' approach were also reported by Dean and Bozzelli [9]. Jodkowski et al. [10] carried out pulse radiolysis experiments and measured rate constants for R1 at 298 K and at pressures in the range of 0.7–1000 mbar. They fitted the measurements in the fall-off region based on the calculated high-pressure (k_∞) and low-pressure limit (k_0) rate constants at 200–400 K, using the methods developed by Troe and co-workers [16,17], and provided expressions as $k_{\infty,\ R1} = 7.13 \times 10^{12}\ T^{0.42}$ cm^3 mol^{-1} s^{-1} and $k_{0,\ R1} = 2.25 \times 10^{30}\ T^{-3.85}$ cm^6 mol^{-2} s^{-1}. Models [13,15] that adopt the $k_{\infty,\ R1}$ and $k_{0,\ R1}$ reported by Jodkowski et al. [10], in combination with a pressure fall-off description in the Lindeman format, are in effect utilizing a rate constant that is 5–19 times faster compared to the Dean and Bozzelli rate constant in the temperature range of 900–1500 K at 20 atm, as shown by the dashed line in Fig. 1. Votsmeier et al. [11] conducted a kinetic measurement in a shock tube for the reverse of R1 (R–1) using the narrow-linewidth laser absorption technique, which allows the initial CH_3NH_2 concentration to be as low as 100 ppm, largely avoiding the perturbation caused by secondary reactions. They determined the rate constant of R–1 at 1.6 and 3.5 atm and 1550–1900 K, and provided a low-pressure limit rate constant expression for $k_{0,\ R\text{–}1}$y= 2.51×10^{16} exp (–56,490/RT) cm^3 mol^{-1} s^{-1} that captures their measurements. However, this expression for R–1 cannot be accurate at lower temperature, as it results in an unreasonably fast reverse rate constant where $k_{0,\ R1} \times$ [M] far exceeds 10^{15} cm^3 mol^{-1} s^{-1} at $T < 1200$ K, as shown by the dotted line in Fig. 1. In a recent modelling study of CH_3NH_2 decomposition by Glarborg and Alzueta [12], a new fit $k_{0,\ R1} = 8.2 \times 10^{34}\ T^{-5.687}$ cm^6 mol^{-2} s^{-1} was generated, based on measurements from both Jodkowski et al. [10] and Votsmeier et al. [11]. In light of the above discussion, it is necessary to determine an accurate rate constant for $\dot{C}H_3 + \dot{N}H_2$ as a function of temperature and pressure, and to provide accurate kinetic data for model development.

In this study, high-level electronic structure calculations are performed to explore the detailed potential energy surface (PES) of the $\dot{C}H_3 + \dot{N}H_2$ reaction and determine rovibrational properties of the stationary points. The barrierless radical-radical reaction channels are treated using sophisticated variable reaction coordinate transition state theory (VRC-TST), based on directly sampled multireference electronic energies. The bottleneck microcanonical rate constants obtained for the barrierless channels are incorporated into a Rice-Ramsperger-Kassel-Marcus/master equation (RRKM/ME) calculation including the complete PES. The calculated pressure-dependent rate constants have been employed in a chemical kinetic model and its implications for modeling NH_3/CH_4 combustion are elucidated.

2. Computational methods

2.1. Potential energy surface calculation

The energies of the stationary points on the $\dot{C}H_3 + \dot{N}H_2$ PES were calculated using the high-level ANL0F method [18], which is a modestly improved version of the ANL0 method [19], based on the optimized geometries and vibrational frequencies obtained using the explicitly correlated CCSD(T)-F12 method [20] with the cc-pVTZ-F12 [21] basis set. Stable products and saddle points on the detailed PES were first explored at the B2PLYP-D3/cc-pVTZ [22,23] level of theory. Intrinsic reaction coordinate (IRC) calculations were performed at the same level of theory for the tight transition states to verify the proper product and reactant connections. Thereafter, except for those involved in marginal reaction channels, all stationary point geometries and vibrational frequencies were re-determined at the CCSD(T)-F12/cc-pVTZ-F12 level of theory. Subsequent reference CCSD(T)/CBS [24] energy calculations and ANL0 correction term determinations were performed based on the CCSD(T)-F12/cc-pVTZ-F12 geometries. Overall, this method provides well converged energies, with typical deviations from the CBS limit of <0.2 kcal mol^{-1}, as shown in a recent study by Klippenstein et al. [18].

The ANL0F energies are obtained using a summation of (i) CCSD(T)/CBS reference energies determined from a simple extrapolation of the results for the aug′-cc-pVQZ and aug′-cc-pV5Z basis sets [19,25], (ii) harmonic zero-point energy (ZPE) corrections at the CCSD(T)-F12/cc-pVTZ-F12 level of theory, (iii) corrections for the effect of higher order excitations (HOEs) obtained at the CCSDT(Q)/cc-pVDZ [26] level of theory, (iv) core-valence (CV) interaction corrections obtained at the CCSD(T)/CBS level of theory from an extrapolation of results for the cc-pcVTZ and cc-pcVQZ [25] basis sets, (v) anharmonic vibrational corrections to ZPE at the B2PLYP-D3/cc-pVTZ level of theory based on the vibrational perturbation theory (VPT2) [27], and (vi) corrections for the relativistic effects employing the Douglas–Kroll–Hess one-electron integrals [28] at the CCSD(T)/aug-cc-pwcVTZ-DK level of theory. The evaluation of the diagonal Born−Oppenheimer correction (DBOC) is not considered in this study due to the marginal contribution of this term in magnitude. Note that two-point formulas, $E_{CBS} = E_{nZ} + \alpha[E_{nZ} - E_{(n-1)Z}]$, are used to obtain all of the CBS extrapolations mentioned above, with extrapolation coefficients $\alpha = 0.75$ for $n = 5$ and $\alpha = 0.50$ for $n = 4$ respectively, as recommended in [19]. Most of these calculations were performed using the Molpro 2015 [29] program, while CCSDT(Q) calculations were performed using the MRCC [30] implementation within Molpro. The density functional theory (DFT) calculations were performed using the Gaussian 09 [31] program.

2.2. Kinetic treatments for the barrierless reaction channels

For the barrierless radical-radical reactions involved in R1–R3, the transition state varies in nature with energy (E) and angular momentum (J) and generally lies at large fragments separation (~2–4 Å), where the interaction energies cannot be accurately evaluated using single-reference methods [32,33]. Moreover, the anharmonic intermolecular motions of the transition state are not well described by either harmonic oscillators or free rotors. The VRC-TST [34–36] method, as implemented in the VaReCoF [37] code, provides highly accurate treatments for these barrierless reactions, yielding rate constant predictions that generally agree with experimental measurements within approximately 20% when interaction energies are generated using an appropriate electronic structure method [32,38]. Therefore, the VRC-TST method is used here.

The VRC-TST method defines transition state dividing surfaces by a fixed distance between pivot points on each of the reacting fragments, where pivot points serve as origins for fragment rotations. The molecular motions within the transition state dividing surfaces are separated into conserved modes and transitional modes, where conserved modes correspond to internal vibrations of the fragments and transitional modes correspond to rotations and relative translations of the fragments. This allows the contribution to the E and J resolved number of states, $N(E,J)$, for conserved and transitional modes to be evaluated differently [39]; the conserved modes are obtained from direct counts over quantized states, while transitional modes are calculated via Monte Carlo phase space integration with a minimization with respect to the dividing surfaces. The full transition state $N^{\ddagger}(E,J)$ is then determined by a convolution of these evaluations.

In the Monte Carlo evaluation of the transitional modes $N(E,J)$ in R1–R3, we employed explicitly correlated complete active space second order perturbation theory (CASPT2-F12) [40] with the cc-pVTZ-F12 basis set, based on a (2e,2o) active space corresponding to the radical orbitals of the separated fragments, for the direct sampling of interaction energies. A sufficiently large number of sampling points was chosen to ensure the convergence of phase space integrals to within a 1σ error bar of $\pm 5\%$. One-dimensional corrections to the interaction energies along the reaction coordinate, obtained from a higher cc-pVQZ-F12 [21] basis set and including the effects of geometry relaxation as the fragments approach each other, are employed. For comparison, the minimum energy paths (MEP) of R1–R3 were also calculated using the explicitly correlated Davidson corrected multireference configuration-interaction (MRCI-F12+QC) [41–43] method with the cc-pVTZ-F12 basis set, as well as using the CASPT2-F12/cc-pVTZ-F12 method with an IPEA shift [44] ("IP" = ionization energy, "EA" = electron affinity), respectively.

For the entrance reaction channel (R1), we find both a singlet and a triplet van der Waals complex (vdW) in the long-range regime using the CASPT2-F12(2e,2o)/cc-pVTZ-F12 method, and four distinct transition states are considered, namely, $\dot{C}H_3 + \dot{N}H_2 \rightleftharpoons$ vdW (TS_1), vdW $\rightleftharpoons CH_3NH_2$ (TS_2), and vdW $\rightleftharpoons$ direct H-atom abstraction reaction products (TS_3 and TS_4). Although the singlet and triplet vdW complexes are nearly degenerate, the spin-orbit coupling in this region is very weak $\sim$0.01 kcal mol^{-1}. Thus, we presume that the singlet and triplet fluxes are disconnected, and we evaluate the singlet and triplet channel reaction rates separately.

For the outer transition state, TS_1, a VRC-TST calculation is performed with the reaction coordinate defined by the distance between the centres-of-mass of the two fragments (ranging from 20 to 8 bohr), to evaluate the singlet state flux. The flux for the triplet state is taken to be three times that flux. For the inner transition state, TS_2, the reaction is presumed to proceed on only the singlet surface. Its flux is evaluated through a separate VRC-TST calculation, and the reaction coordinate is defined by the distance between the pivot points on the two fragments (ranging from 8 to 4 bohr with a grid spacing of 0.5 bohr). For both $\dot{C}H_3$ and $\dot{N}H_2$, two pivot points are displaced above and below the molecular plane for each fragment, along the radical orbitals with displacements of 0.01, 0.5 and 1.0 bohr. A dynamical recrossing correction factor of 0.85 is employed for the entrance addition reaction channel as obtained from direct trajectory simulations for $\dot{C}H_3 + \dot{C}H_3$ [38].

There is still an important question regarding whether or not the vdW complexes lead to a statistical exploration of their phase space. Here, since the vdW complexes have relatively modest binding energies ($\sim$0.3 kcal mol^{-1}), we presume that the trajectories pass through this region more or less directly. In this instance, the overall transition state flux is taken as the minimum of the two separate TS fluxes; i.e., of the TS_1 flux to form the vdW complex and the TS_2 flux for that vdW complex to proceed to a chemically bound complex.

For the two barrierless decomposition channels, R2 and R3, the transition state dividing surfaces are again defined by the distance between the centres of mass at a separation $\geq$8 bohr. While at a separation of $<$8 bohr, one pivot point is placed at the nucleus of the $\dot{H}$ atom, and two pivot points are placed along the radical orbitals of $\dot{C}H_2NH_2$/$CH_3\dot{N}H$, atop and beneath the C/N atom with displacements of 0.5, 1.0 and 1.5 bohr considered. A dynamical correction factor of 0.9 is adopted, as recommended by Harding et al. [33] based on a comparison with previous trajectory studies of alkyl + $\dot{H}$. The transitional mode number of states as a function of energy obtained from the VRC-TST calculations for R1–R3 are incorporated into the subsequent master equation calculation.

2.3. Rate constants calculation

An RRKM/ME calculation was performed to obtain the temperature- and pressure-dependent phenomenological rate constants for addition and subsequent reaction pathways of $\dot{C}H_3 + \dot{N}H_2$, while the H-atom abstraction reaction pathways were treated using conventional transition state theory [45,46]. The rovibrational properties of the stationary points obtained at the CCSD(T)-F12/cc-pVTZ-F12 level of theory are employed with the rigid-rotor harmonic-oscillator (RRHO) model to determine the number of states for the internal degrees of freedom of stable species and tight transition states. The normal mode vibrational frequencies were obtained at the CCSD(T)-F12/cc-pVTZ-F12 level of theory and corrected with the difference between anharmonic and harmonic vibrational frequencies obtained at the B2PLYP-D3/cc-pVTZ level of theory. The low-frequency torsional modes are treated as one-dimensional hindered rotors (1-D HR), with the hindrance rotational potentials scanned at the CCSD(T)-F12/cc-pVTZ-F12 level of theory. The asymmetric Eckart model [47] is used to characterize the tunnelling corrections for all tight transition states. In the master equation calculation, the collision rates are evaluated based on the Lennard-Jones (L-J) potential. The L-J parameters, $\sigma = 5.26$ Å and $\varepsilon = 254.8$ cm^{-1}, estimated for CH_3NH_2 using group additivity by RMG [48] are adopted with N_2 as the bath gas. The collisional energy transfer is described using the single exponential down model, with the averaged downward energy transferred per collision estimated as $\langle \Delta E_d \rangle = 90\,(T/300)^{1.0}$ cm^{-1}. The Master Equation System Solver (MESS) [49,50] code was used to carry out these rate constant calculations. The calculated rate constants are provided as Supplementary material (SM).

2.4. Thermochemical properties calculation

The thermochemical properties were calculated for CH_3NH_2, $\dot{C}H_2NH_2$, $CH_3\dot{N}H$ and $^1CHNH_2$ as a function of temperature and pressure. Their enthalpies of formation at 0 K ($\Delta H_{f,0\,K}$) were calculated using the atomization approach, based on the $\Delta H_{f,0\,K}$ for C, N, and H atoms from the Active Thermochemical Tables (ATcT) [51] and the binding energies were calculated using the ANL0F method, as described in Section 2.1. Here, the CCSD(T)/CBS reference energies in the ANL0F scheme were determined based on the extrapolation formula, $E_{CBS} =$

$1.779E_{a'nZ} - 0.779E_{a'(n-1)Z}$, as recommended by Elliot et al. [52]. In the molecular partition function calculation, similar treatments as in the rate constant calculation were used, with corrections from the VPT2 calculations included for the normal mode vibrational frequencies to account for anharmonicity, and 1-D HR model employed for the internal rotations. Additionally, the partition functions for the umbrella vibrational modes of the –NH_2 and –$\dot{C}H_2$ groups in CH_3NH_2, $\dot{C}H_2NH_2$ and $^1CHNH_2$ were determined based on their 1-D inversion potentials, as was that for $\dot{C}H_3$. These umbrella mode inversion potentials are also employed in the rate constant calculations. The temperature-dependent enthalpies (H), entropies (S) and heat capacities (C_p) were obtained and fitted to NASA polynomials via calls to the ThermP [53] and PAC99 [54] codes, based on the determined molecular partition functions using the MESS code. The calculated thermochemical data are provided as SM.

3. Results and discussion

3.1. Detailed reaction pathways

The calculated potential energy surface for $\dot{C}H_3 + \dot{N}H_2$ is illustrated in Fig. 2. The bimolecular reactants first form a van der Waals complex (vdW) at a C–N distance of ~3.5 Å, with its energy being 0.3 kcal mol^{-1} below the $\dot{C}H_3 + \dot{N}H_2$ asymptote, via a barrierless entrance channel. The triplet vdW can proceed through two direct H-atom abstraction saddle points, with energy barriers of 9.1 and 13.7 kcal mol^{-1}, giving CH_4 + ^3NH and $^3CH_2 + NH_3$, respectively. While the fragments in the singlet complex can proceed to form the stable molecule methylamine (CH_3NH_2), which is stabilized at –82.5 kcal mol^{-1} relative to the reactants, via a barrierless addition channel. CH_3NH_2 can then undergo barrierless C–H and N–H bond fission reactions, forming $\dot{C}H_2NH_2 + \dot{H}$ and $CH_3\dot{N}H + \dot{H}$ at 8.8 and 15.8 kcal mol^{-1} above the $\dot{C}H_3 + \dot{N}H_2$ asymptote, respectively. It can also undergo H_2 elimination reactions, where H_2 elimination from the methyl group forming $^1CHNH_2 + H_2$ is the most energetically favoured reaction channel, with an electronic energy barrier of 79.2 kcal mol^{-1}. Elimination of H_2 from the amino group and concerted elimination of H_2 from the methyl and amino groups are unlikely to be important, with their transition states being 113.2 and 104.0 kcal mol^{-1} respectively. The IRC calculation shows that CH_3N, formed from the H_2 elimination of the amino group, is unstable and immediately isomerizes to CH_2NH. Therefore, both TSs connect to $CH_2NH + H_2$.

We examined the coupled cluster electronic energies for the stationary points on the $\dot{C}H_3 + \dot{N}H_2$ PES in terms of their convergence with respect to the basis set, Table 1. The average deviations of the CCSD(T)-F12 energies for the cc-pVTZ-F12 (TZ-F12) and cc-pVQZ-F12 (QZ-F12) basis sets from the CBS limits are, ~0.09 and ~0.05 kcal mol^{-1}, respectively, with maximum deviations of 0.29 and 0.15 kcal mol^{-1}. Meanwhile, the $CBS_{T,QZF}$ and $CBS_{a'Q,5Z}$ energies agree within 0.07 kcal mol^{-1} of one another. This indicates that the coupled cluster electronic energies results are well converged with respect to the basis set. The $CBS_{a'Q,5Z}$ results are used as reference energies for the ANL0F energy calculations.

The calculated ANL0F stationary point energies with the values for all correction terms are shown in Table 2. The T1 diagnostics for all stationary points studied are <0.018, indicating a minor effect of the multireference character on their energy results. The tight transition states for the H_2 elimination and H-atom abstraction pathways show relatively larger absolute values for the CCSDT(Q)/cc-pVDZ correction, it being up to 0.41 kcal mol^{-1}. We also determined the energy barriers using multireference methods for these pathways, based on optimized geometries and ZPEs obtained at the CASPT2-F12/cc-pVTZ-F12 level of theory, Table 3. The difference between the energy barriers obtained using the CASPT2-F12 and MRCI-F12+QC methods for these channels is ~2.2 kcal mol^{-1}, with the MRCI-F12+QC method always predicting larger barriers. The electronic energy barriers obtained using the ANL0F method lie between the results from CASPT2-F12 and MRCI-F12+QC, with average differences of 1.4 and 0.9 kcal mol^{-1}, respectively. The CASPT2-F12 energies evaluated with an IPEA shift are slightly closer to the ANL0F energies. Since the higher order excitation energies were never overly large, the ANL0F energy barriers were used in the kinetic calculations, including those for the saddle points listed in Table 3. The mean values of higher-order excitation, core-valence, anharmonicity,

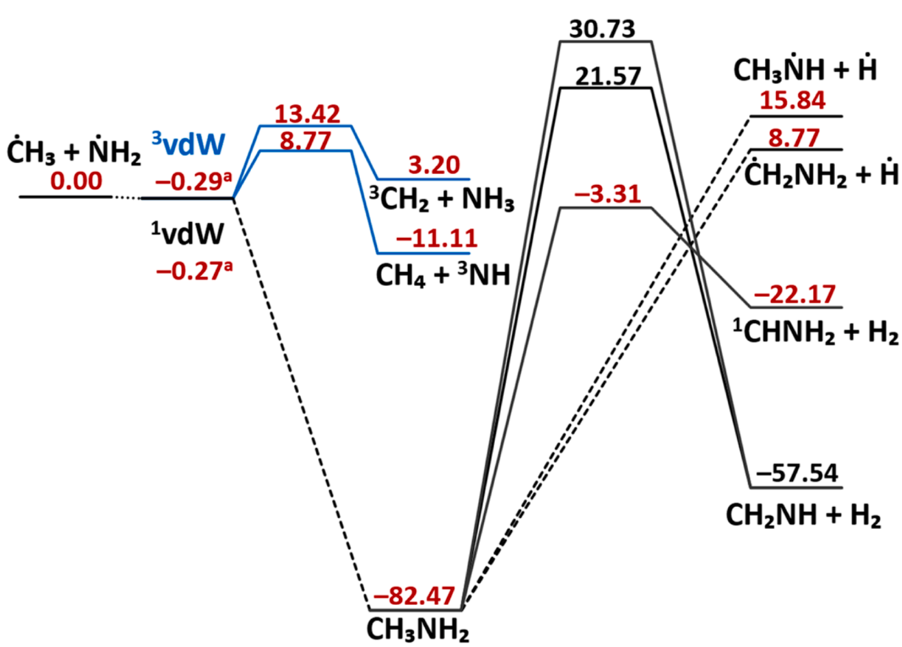

Fig. 2. The calculated potential energy surface for $\dot{C}H_3 + \dot{N}H_2$ (kcal mol^{-1}). Energy values are displayed in red for ANL0F ([a] CASPT2-F12(2e,2o)/cc-pVTZ-F12) and in black for CCSD(T)-F12/cc-pVTZ-F12//B2PLYP-D3/cc-pVTZ. The solid lines denote reactions with a tight transition state, while dashed lines denote barrierless reactions; the black colour indicates the singlet reaction channels, while the blue colour corresponds to the triplet reaction channels.

Table 1
Basis set convergence of coupled cluster energies for $\dot{C}H_3 + \dot{N}H_2$ (kcal mol^{-1}).

Stationary point	CCSD(T)-F12					CCSD(T)		
	DZ-F12	TZ-F12	QZ-F12	$CBS_{D,TZF}$[a]	$CBS_{T,QZF}$[b]	a′QZ	a′5Z	$CBS_{a'Q,5Z}$[c]
$\dot{C}H_3 + \dot{N}H_2$	0	0	0	0	0	0	0	0
CH_3NH_2	–91.22	–91.42	–91.61	–91.50	–91.71	–90.69	–91.23	–91.64
$CH_3NH_2 \rightleftharpoons {}^1CHNH_2 + H_2$	–5.09	–5.35	–5.49	–5.46	–5.56	–4.52	–5.07	–5.49
${}^1CHNH_2 + H_2$	–22.60	–22.53	–22.61	–22.49	–22.65	–21.84	–22.27	–22.60
$\dot{C}H_3 + \dot{N}H_2 \rightleftharpoons CH_4 + {}^3NH$	8.78	8.78	8.85	8.78	8.89	8.80	8.84	8.87
$CH_4 + {}^3NH$	–13.97	–13.30	–13.18	–13.03	–13.11	–13.61	–13.35	–13.16
$\dot{C}H_3 + \dot{N}H_2 \rightleftharpoons {}^3CH_2 + NH_3$	13.86	13.67	13.66	13.60	13.66	13.77	13.70	13.64
${}^3CH_2 + NH_3$	1.54	1.70	1.64	1.76	1.61	1.67	1.63	1.60
$\dot{C}H_2NH_2 + \dot{H}$	8.63	8.55	8.45	8.51	8.40	9.15	8.76	8.47
$CH_3\dot{N}H + \dot{H}$	15.75	15.89	15.89	15.94	15.89	16.37	16.13	15.95

[a] The CCSD(T)-F12/CBS energies obtained by $E_{\text{CCSD(T)-F12/cc-pVTZ-F12}} + 0.4 \times (E_{\text{CCSD(T)-F12/cc-pVTZ-F12}} - E_{\text{CCSD(T)-F12/cc-pVDZ-F12}})$.
[b] The CCSD(T)-F12/CBS energies obtained by $E_{\text{CCSD(T)-F12/cc-pVQZ-F12}} + 0.5 \times (E_{\text{CCSD(T)-F12/cc-pVQZ-F12}} - E_{\text{CCSD(T)-F12/cc-pVTZ-F12}})$.
[c] The CCSD(T) /CBS energies obtained by $E_{\text{CCSD(T)/aug'-cc-pV5Z}} + 0.75 \times (E_{\text{CCSD(T)/aug'-cc-pV5Z}} - E_{\text{CCSD(T)/aug'-cc-pVQZ}})$.

Table 2
Components of the ANL0F energies for $\dot{C}H_3 + \dot{N}H_2$ (kcal mol^{-1}).

Stationary point	CCSD(T)/CBS[a]	ZPE[b]	HOE[c]	CV[d]	Anh.[e]	Rel.[f]	Total[g]
$\dot{C}H_3 + \dot{N}H_2$	0	0	0	0	0	0	0
CH_3NH_2	–91.64	9.63	0.02	–0.34	–0.28	0.15	–82.47
$CH_3NH_2 \rightleftharpoons {}^1CHNH_2 + H_2$	–5.49	2.89	–0.41	–0.08	–0.32	0.10	–3.31
${}^1CHNH_2 + H_2$	–22.60	0.64	–0.16	0.02	–0.12	0.05	–22.17
$\dot{C}H_3 + \dot{N}H_2 \rightleftharpoons CH_4 + {}^3NH$	8.87	0.17	–0.20	0.10	–0.13	–0.03	8.77
$CH_4 + {}^3NH$	–13.16	2.12	0.07	0.03	–0.10	–0.07	–11.11
$\dot{C}H_3 + \dot{N}H_2 \rightleftharpoons {}^3CH_2 + NH_3$	13.64	0.15	–0.21	0.07	–0.26	0.02	13.42
${}^3CH_2 + NH_3$	1.60	1.77	0.02	–0.07	–0.21	0.08	3.20
$\dot{C}H_2NH_2 + \dot{H}$	8.47	0.85	–0.02	–0.38	–0.29	0.14	8.77
$CH_3\dot{N}H + \dot{H}$	15.95	0.09	–0.02	–0.10	–0.12	0.04	15.84

[a] The CCSD(T) /CBS energies obtained by $E_{\text{CCSD(T)/aug'-cc-pV5Z}} + 0.75 \times (E_{\text{CCSD(T)/aug'-cc-pV5Z}} - E_{\text{CCSD(T)/aug'-cc-pVQZ}})$.
[b] The harmonic zero-point energy corrections obtained at the CCSD(T)-F12/cc-pVTZ-F12 level.
[c] The higher-order excitation corrections obtained by the energy difference between UHF-UCCSDT(Q)/cc-pVDZ and RHF-UCCSD(T)/cc-pVDZ.
[d] The core-valence corrections obtained by a CBS extrapolation of energy difference (ΔE_{CV}) between CCSD(T,full) and CCSD(T), for cc-pcVQZ and cc-pcVTZ basis sets, using the formula $\Delta E_{\text{CV, cc-pcVQZ}} + 0.5 \times (\Delta E_{\text{CV, cc-pcVQZ}} - \Delta E_{\text{CV, cc-pcVTZ}})$.
[e] The anharmonic zero-point energy corrections obtained at the B2PLYP-D3/cc-pVTZ level.
[f] The relativistic corrections obtained at the CCSD(T)/aug-cc-pwcVTZ-DK level.
[g] The total ANL0F energies given by the sum of all the terms above.

and relativistic corrections in Table 2 are 0.11, 0.12, 0.18 and 0.07 kcal mol^{-1}, respectively, with maximum values of 0.41, 0.38, 0.32 and 0.15 kcal mol^{-1}. The maximum absolute value for the sum of these four correction terms is observed for the saddle point of $CH_3NH_2 \rightleftharpoons {}^1CHNH_2 + H_2$, as 0.71 kcal mol^{-1}.

In Table 4 we compare the calculated stationary point energies at ANL0F and CCSD(T)-F12/cc-pVTZ-F12//B2PLYP-D3/cc-pVTZ levels of theory with those determined based on the available stable species $\Delta H_{f,0\ K}$ from the ATcT [51]. The average deviations from the ATcT values for the ANL0F and CCSD(T)-F12/cc-pVTZ-F12//B2PLYP-D3/cc-pVTZ methods are 0.05 and 0.21 kcal mol^{-1}, respectively. The level of agreement between the ANL0F energies and the ATcT values for the reaction products here is typically within 0.1 kcal mol^{-1}. Although a deviation of 0.26 kcal mol^{-1} is observed for $CH_3\dot{N}H + \dot{H}$, this may be indicative of an error in the ATcT $\Delta H_{f,0\ K}$ for $CH_3\dot{N}H$, although the stated uncertainty in the ATcT CH_3NH value is 0.10 kcal mol^{-1}. Since the CCSDT(Q)/cc-pVDZ corrections for all saddle points are below 0.41 kcal mol^{-1}, we can expect the ANL0F energies for the saddle points to have similar uncertainties as those for the stable products [18].

Table 3
Comparison of the calculated multireference energies with ANL0F values for the tight transition states (in kcal mol^{-1}).

Stationary point[a]	CASPT2-F12/cc-pVTZ-F12			MRCI-F12+QC/cc-pVTZ-F12		ANL0F
	Energy[b]	ZPE	Total[c]	Energy[b]	Total[d]	Total
$CH_3NH_2 \rightleftharpoons {}^1CHNH_2 + H_2$	15.21 (15.80)	1.94 (2.09)	17.15 (17.89)	17.11	19.05	18.86
$\dot{C}H_3 + \dot{N}H_2 \rightleftharpoons CH_4 + {}^3NH$	20.44 (21.76)	–2.00 (–1.96)	18.43 (19.81)	23.22	21.21	19.88
$\dot{C}H_3 + \dot{N}H_2 \rightleftharpoons {}^3CH_2 + NH_3$	10.90 (12.48)	–1.59 (–1.64)	9.32 (10.84)	12.92	11.34	10.22

[a] Stationary point energy relative to ${}^1CHNH_2 + H_2$, $CH_4 + {}^3NH$ and ${}^3CH_2 + NH_3$, based on active spaces of (2e,2o), (4e,4o) and (4e,4o) in the multireference calculations, respectively.
[b] Electronic energy calculated at the CASPT2-F12/cc-pVTZ-F12 geometry; values outside/inside the parentheses are from regular/IPEA level shift, respectively.
[c] Sum of the energy and zero-point energy correction at CASPT2-F12/cc-pVTZ-F12.
[d] Sum of the energy at MRCI-F12+QC/cc-pVTZ-F12 and zero-point energy correction at CASPT2-F12/cc-pVTZ-F12.

Table 4
Comparison of calculated relative energies with ATcT values [51] (in kcal mol^{-1}).

Stationary point	CC-F12//B2[a]	Dev.[b]	ANL0F	Dev.[c]	ATcT	ATcT Unc.[d]
$\dot{C}H_3 + \dot{N}H_2$	0	0	0	0	0	0
CH_3NH_2	–81.85	0.67	–82.47	0.05	–82.52	0.09
$CH_3NH_2 \rightleftharpoons {}^1CHNH_2 + H_2$	–2.17		–3.31			
${}^1CHNH_2 + H_2$	–21.88	0.32	–22.17	0.03	–22.20	0.40
$\dot{C}H_3 + \dot{N}H_2 \rightleftharpoons CH_4 + {}^3NH$	9.10		8.77			
$CH_4 + {}^3NH$	–11.18	–0.04	–11.11	0.03	–11.14	0.09
$\dot{C}H_3 + \dot{N}H_2 \rightleftharpoons {}^3CH_2 + NH_3$	14.03		13.42			
${}^3CH_2 + NH_3$	3.45	0.18	3.20	–0.07	3.27	0.07
$\dot{C}H_2NH_2 + \dot{H}$	9.35	0.59	8.77	0.01	8.76	0.12
$CH_3\dot{N}H + \dot{H}$	15.90	0.32	15.84	0.26	15.58	0.13

[a] The energies obtained at the CCSD(T)-F12/cc-pVTZ-F12//B2PLYP-D3/cc-pVTZ level.
[b] Deviations between the CC-F12//B2 and ATcT values.
[c] Deviations between the ANL0F and ATcT values.
[d] ATcT uncertainties obtained from individual species uncertainties.

3.2. Minimum energy paths for the barrierless reaction channels

Fig. 3 illustrates the calculated minimum energy paths (MEP) for the barrierless reaction channels, spanning the intermolecular separations typical of the transition state region. The MEPs were first calculated with the internal structures of the two fragments held fixed and were then recalculated with the fragment structures allowed to be fully optimized (relaxed). The geometry relaxation corrections are obtained as the energy differences between the relaxed and fixed MEPs. This correction was determined at the CASPT2-F12(2e,2o)/cc-pVTZ-F12 level of theory and generally results here in corrections to the interaction energies of <6% in the short-range transition state region. The obtained CASPT2-F12 interaction energies are again well converged with respect to the basis set, as the results for the cc-pVQZ-F12 and cc-pVTZ-F12 basis sets differ by $\leq$ 0.05 kcal mol^{-1}. Inclusion of the IPEA shift generally results in energy differences of < 5% for $\dot{C}H_3 + \dot{N}H_2 \rightleftharpoons CH_3NH_2$, and differences of < 10% for the other two barrierless reaction channels. The MRCI-F12 calculations yields a slightly larger difference of 10–20% from the CASPT2-F12 energies. We can expect a similar percentage deviation in the rate constants calculated from the MEPs for the MRCI-F12 and CASPT2-F12 (with IPEA shift) energies compared to those from CASPT2-F12 (without IPEA shift). Our VRC-TST results are based on the CASPT2-F12 MEPs (without IPEA shift). With these small deviations we expect 2σ uncertainties on the order of 20% for each of the predictions for the high-pressure recombination rate constants for the barrierless channels.

3.3. Rate constants

The calculated temperature- and pressure-dependent rate constants for the entrance addition reaction channel (R1) and its reverse

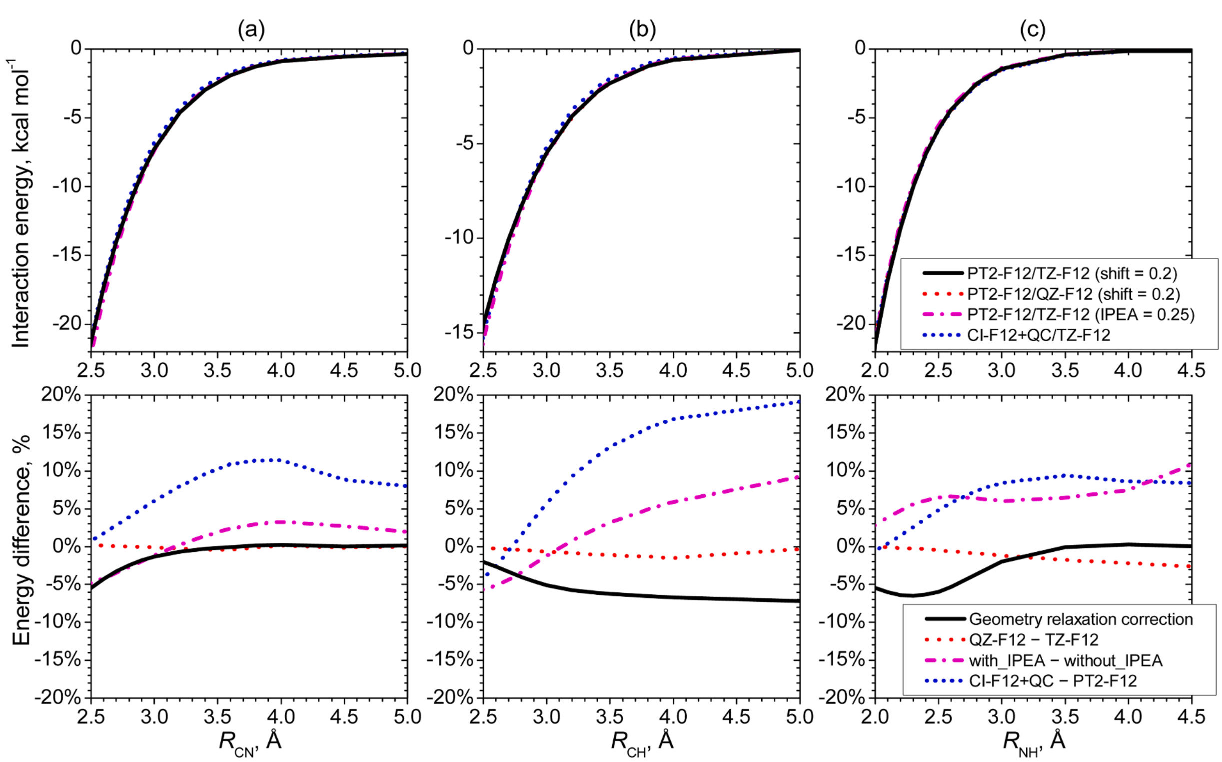

Fig. 3. The calculated MEPs using different multireference methods, based on a (2e,2o) active space, and their energy difference for (a) $\dot{C}H_3 + \dot{N}H_2 \rightleftharpoons CH_3NH_2$, (b) $\dot{C}H_2NH_2 + \dot{H} \rightleftharpoons CH_3NH_2$, and (c) $CH_3\dot{N}H + \dot{H} \rightleftharpoons CH_3NH_2$.

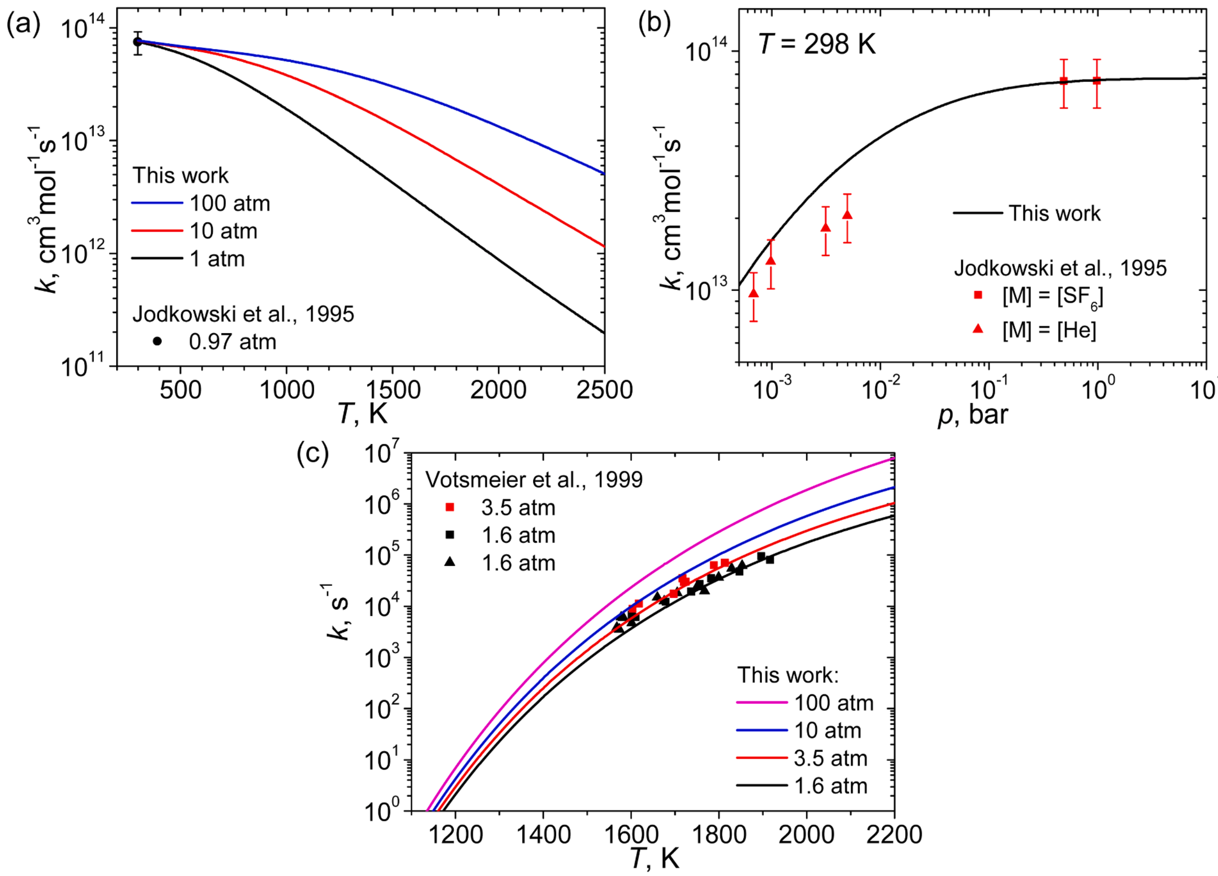

Fig. 4. The calculated (a) rate constant and (b) pressure fall-off curve at 298 K for $\dot{C}H_3 + \dot{N}H_2 \rightleftharpoons CH_3NH_2$, and (c) rate constant for $CH_3NH_2 \rightleftharpoons \dot{C}H_3 + \dot{N}H_2$, compared with available kinetic measurements [10,11] in the literature.

decomposition process (R–1) are shown in Fig. 4, and are compared to available kinetic measurements [10,11] from the literature. Our calculated rate constant for R1 is in good agreement with those measured by Jodkowski et al. [10] at room temperature and in the pressure range 0.005–1 bar, Fig. 4(a) and Fig. 4(b). At 298 K, the rate constant for R1 approaches its high-pressure limit at pressures above 1 atm, while it shows a more pronounced pressure falloff character at 1000 K and above. Again, our calculated rate constant for R–1 captures very well the

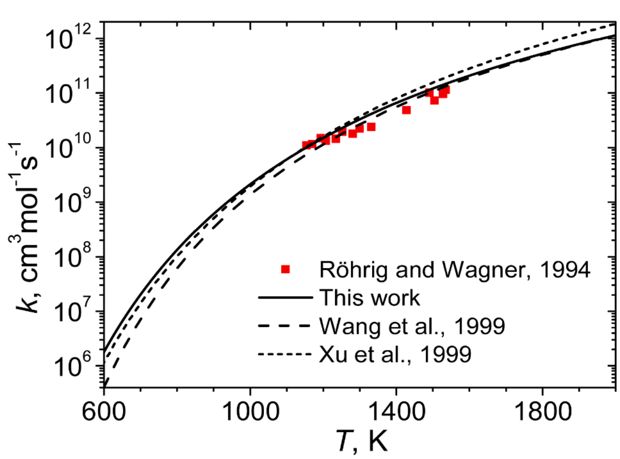

Fig. 5. The calculated rate constant for $CH_4 + {}^3NH \rightleftharpoons \dot{C}H_3 + \dot{N}H_2$, compared with available calculation results [56,57] and kinetic measurements [55] in the literature.

measured data by Votsmeier et al. [11] at 1.6, 3.5 atm and in the temperature range 1550–1900 K, Fig. 4(c). Fig. 5 shows our calculated rate constant for R–4, compared to measured data from Röhrig and Wagner [55] and calculations from Wang et al. [56] and Xu et al. [57]. All three calculations for R–4 are generally within 25% of one another in the temperature range of 800–2000 K and are in good agreement with the experimental data.

The rate constants obtained from the RRKM/ME calculation and the corresponding product branching ratios at 1, 10 and 100 atm for $\dot{C}H_3 + \dot{N}H_2 \rightleftharpoons$ products are shown in Fig. 6. At temperatures below 1400 K, the stabilization to CH_3NH_2 (R1) is dominant and this stabilization strengthens with increasing pressure. At 1500 K, the formation of the bimolecular products $\dot{C}H_2NH_2 + \dot{H}$ (R2) via a chemically activated reaction pathway starts to compete with R1, and it dominates at temperatures above 2000 K. The ratio of $^1CHNH_2 + H_2$ (R6) formation increases to about 8% at ~1500 K and 1 atm. This decreases at higher temperatures and pressures. The ring structure of the transition state for the H_2 elimination reaction channel R6 results in a higher entropy cost at the saddle point, making this reaction channel less competitive at high temperatures. The direct H-atom abstraction reaction channels R4 and R5 are of minor importance with relative ratios of < 15% over the entire temperature range. The formations of $CH_3\dot{N}H + \dot{H}$ (R3) and $CH_2NH + H_2$ (R7) are negligible due to their significantly higher threshold energies.

The calculated unimolecular reaction rate constants for $CH_3NH_2 \rightleftharpoons$ products at 10 atm are shown in Fig. 7. Under combustion-relevant conditions, dissociation to form $\dot{C}H_3 + \dot{N}H_2$ via R–1 is dominant over the other unimolecular reaction pathways of CH_3NH_2, with its rate constant being more than ~40 times faster. It is likely that the CH_3NH_2 produced from $\dot{C}H_3 + \dot{N}H_2$ will undergo bimolecular oxidation reactions with species in the radical pool. The calculated rate constants for $\dot{C}H_3$ +

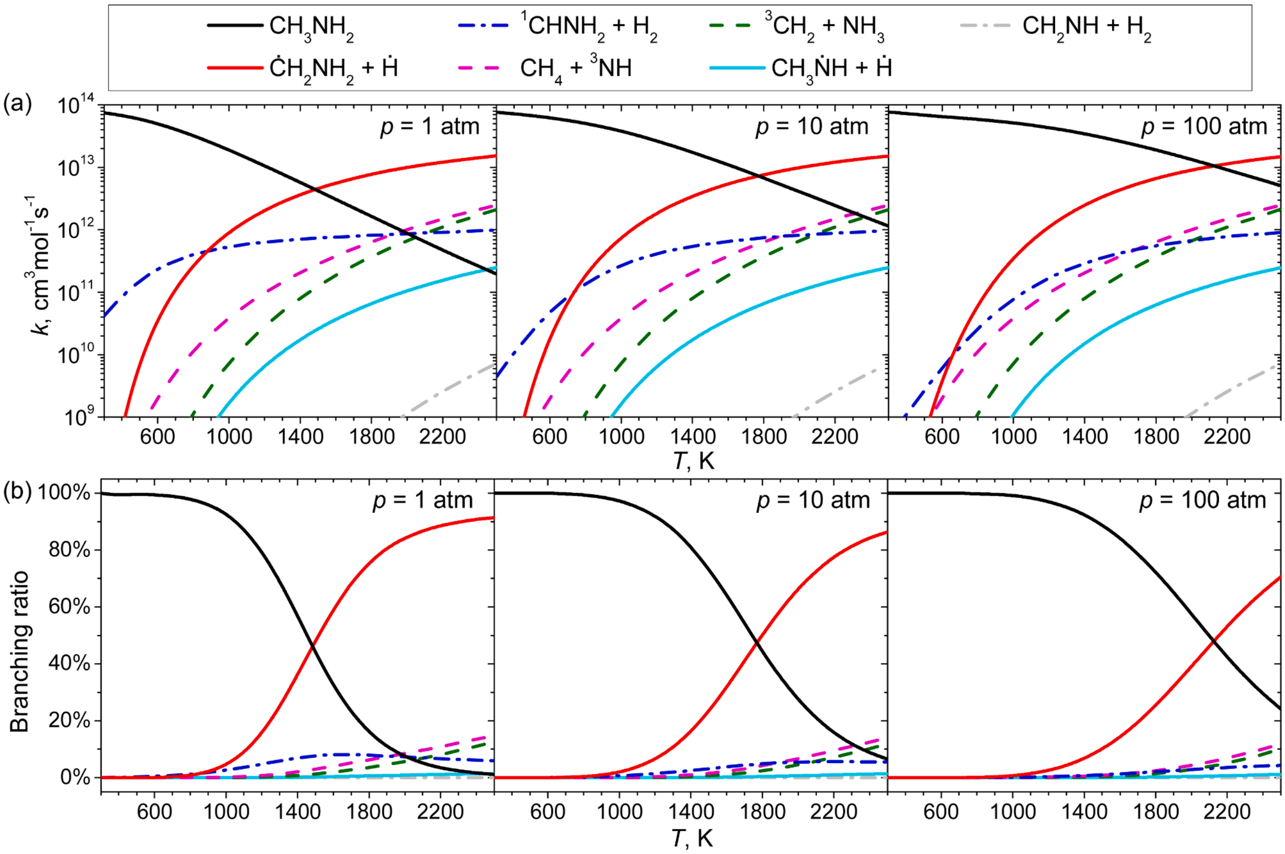

Fig. 6. The calculated (a) rate constants and (b) product branching ratios for $\dot{C}H_3 + \dot{N}H_2 \rightleftharpoons$ products.

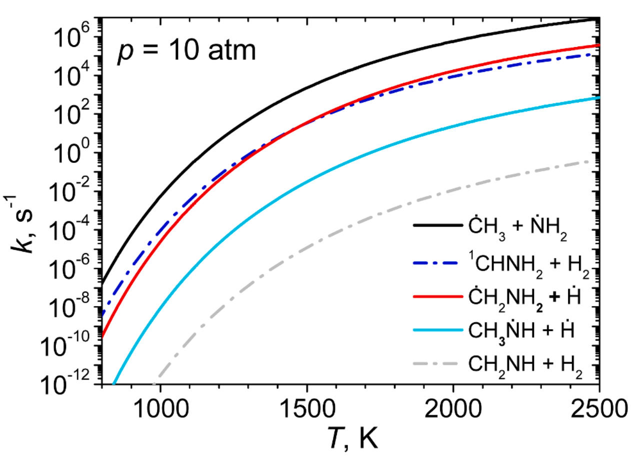

Fig. 7. The calculated rate constants for $CH_3NH_2 \rightleftharpoons$ products at 10 atm.

$\dot{N}H_2 \rightleftharpoons$ products and $CH_3NH_2 \rightleftharpoons$ products are fitted using modified Arrhenius expression and are provided as SMM.

3.4. Thermochemical properties

Our calculated thermochemical properties, based on $\Delta H_{f,0\ K}$ results determined from the ANL0F energies and species geometries and rovibrational properties determined at the CCSD(T)-F12/cc-pVTZ-F12 level of theory, are shown in Table 5. These are also compared with the ATcT [51] values and calculation results from Bugler et al. [58]. The ANL0F $\Delta H_{f,0\ K}$ show a similar level of agreement with the ATcT values as observed for the PES, typically being within 0.1 kcal mol^{-1}. This yields $\Delta H_{f,298\ K}$ results that are also in good agreement with the ATcT values. Note that the $\Delta H_{f,0\ K}$ values determined by Bugler et al. from an average of CBS-APNO, G3 and G4 compound method energies also provide good predictions for CH_3NH_2 and $CH_3\dot{N}H$, being within 0.1 kcal mol^{-1} of the ANL0F $\Delta H_{f,0\ K}$ values, although the deviation for $\dot{C}H_2NH_2$ is slightly larger, at 0.4 kcal mol^{-1}. The differences in $H(T)$, $S(T)$ and $C_p(T)$ between this work and the study of Bugler et al. arise from the use of different geometries and rovibrational properties for the molecular partition function calculations, with Bugler et al. employing the B3LYP/cc-pVTZ method. The different treatments for the umbrella modes used here result in quite similar calculated thermochemical properties for CH_3NH_2 and $^1CHNH_2$. However, for $\dot{C}H_2NH_2$, the differences in the calculated $H(T)$, $S(T)$ and $C_p(T)$ between the two treatments become 1.9 kcal mol^{-1}, 3.0 and 1.3 cal mol^{-1} K^{-1} at 2000 K, respectively. This discrepancy arises from the coupling of the two umbrella modes and the torsional mode in $\dot{C}H_2NH_2$.

3.5. Implications for NH_3/CH_4 combustion kinetic modeling

The calculated rate constants for $\dot{C}H_3 + \dot{N}H_2 \rightleftharpoons$ products and $CH_3NH_2 \rightleftharpoons$ products, in addition to their species thermochemistry data with a proper umbrella mode treatment, were incorporated into a NH_3/CH_4 chemical kinetic model under development at the University of Galway. It is developed based on our published NH_3/H_2 mechanism [59] and C_2 subsets as part of GalwayMech1.0 [60]. Before updating these kinetic data in the model, the rate constant expressions for R1 were adopted from Jodkowski et al. [10], while those for R2–R5 and R7 were all taken from Dean and Bozzelli [9]. Furthermore, the product channel forming $^1CHNH_2 + H_2$ (R6) was not included in the model. Simulations were conducted using both the updated and original models and compared against NH_3/CH_4 IDT data measured in shock tubes [61,62] and in rapid compression machines (RCMs) [6,7] reported in the

Table 5
The calculated thermochemical properties (with units of K for T, kcal mol^{-1} for H, and cal mol^{-1} K^{-1} for S and C_p).

Species	$\Delta H_f(0)$	ΔH_f°	S°	$C_p(T)$				
				300	500	1000	1500	2000
CH_3NH_2	−1.48[a], −1.54[b]	−5.0[a], −5.1[b]	58.0[a]	11.8[a]	16.5[a]	25.2[a]	29.8[a]	32.3[a]
		−5.0[c]	58.0[c]	12.0[c]	16.7[c]	25.1[c]	29.5[c]	31.9[c]
	−1.47[d]	−5.0[d]	57.9[d]	11.8[d]	16.5[d]	25.5[d]	30.5[d]	33.3[d]
$\dot{C}H_2NH_2$	38.13[a], 38.10[b]	35.7[a], 35.7[b]	59.1[a]	13.1[a]	16.7[a]	22.7[a]	26.2[a]	28.0[a]
		35.8[c]	58.2[c]	12.4[c]	15.7[c]	21.5[c]	24.9[c]	26.7[c]
	38.57[d]	36.4[d]	61.5[d]	13.5[d]	17.0[d]	21.5[d]	24.3[d]	26.0[d]
$CH_3\dot{N}H$	45.20[a], 44.92[b]	42.6[a], 42.4[b]	58.7[a]	10.9[a]	14.7[a]	21.9[a]	25.6[a]	27.5[a]
	45.17[d]	42.6[d]	58.7[d]	10.9[d]	14.8[d]	22.1[d]	25.9[d]	27.9[d]
$^{1}CHNH_2$	58.81[a], 58.77[a]	56.9[a], 56.9[b]	54.4[a]	9.5[a]	12.8[a]	18.5[a]	21.5[a]	23.0[a]
		56.9[c]	54.4[c]	9.4[c]	12.7[c]	18.4[c]	21.3[c]	22.8[c]

[a] The umbrella modes for the $-NH_2$ and $-\dot{C}H_2$ groups were treated as harmonic oscillators.
[b] ATcT [51] values.
[c] The umbrella modes for the $-NH_2$ and $-\dot{C}H_2$ groups were treated as separated 1-D inversions.
[d] Values reported from the study of Bugler et al. [58].

literature. All simulations were performed using the Cantera [63] solver, assuming constant-volume for shock tube data and using volume profiles to account for heat loss in RCM data.

Fig. 8 shows the effect of the updated $\dot{C}H_3 + \dot{N}H_2$ and CH_3NH_2 rate constants on our model-predicted NH_3/CH_4 low-temperature IDTs in RCMs, depending on equivalence ratio, pressure, and CH_4 mole fraction in the blend. The predicted low-temperature fuel reactivities of NH_3/CH_4 mixtures consistently increase by approximately 45% in varying

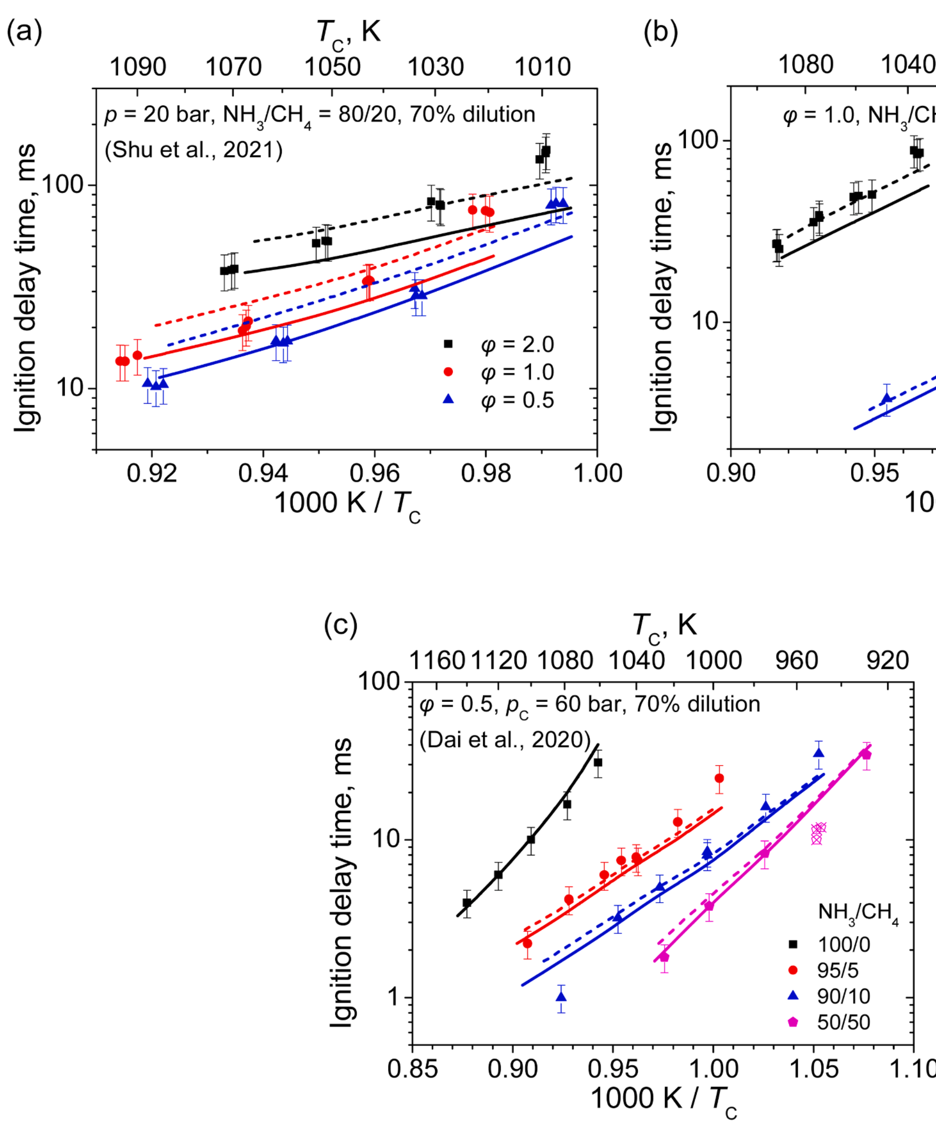

Fig. 8. Low-temperature IDTs of NH_3/CH_4 mixtures (a) at different equivalence ratios 0.5–2.0, (b) at different pressures 20–40 bar, and (c) at different CH_4 mole fractions 0–50%. Symbols: RCM experimental data [6,7] from the literature. Solid lines: updated model predictions, dashed lines: original model predictions.

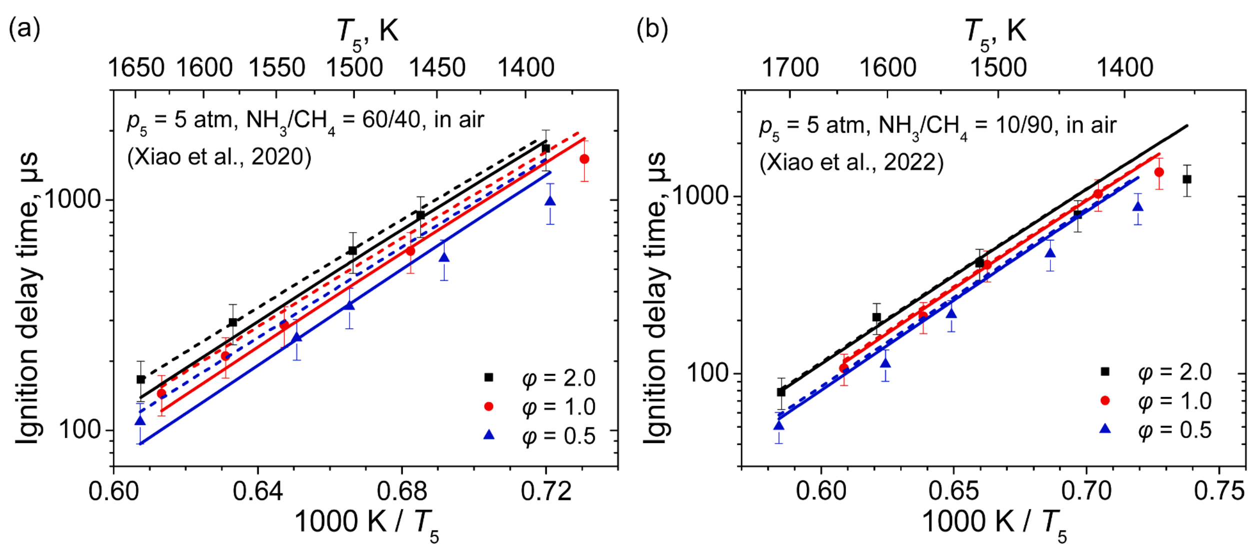

Fig. 9. High-temperature IDTs of NH_3/CH_4 mixtures at different equivalence ratios 0.5–2.0 for (a) 60/40 and (b) 10/90 blending ratios. Symbols: shock tube experimental data [61,62] from the literature. Solid lines: updated model predictions, dashed lines: original model predictions.

from fuel-lean, through stoichiometric to fuel-rich conditions, Fig. 8(a); a larger difference in the predicted IDTs is observed for lower-pressure conditions compared to higher-pressure conditions, Fig. 8(b). Among the NH_3/CH_4 mixtures with blending ratios of 95/5, 90/10, and 50/50, the largest reactivity-enhancing effect is observed for the 90/10 blend, with this effect being more pronounced at temperatures greater than 1100 K, Fig. 8(c). In the high-temperature combustion regime, Fig. 9, the predicted shock tube IDTs for the 60/40 NH_3/CH_4 blend again increase with equivalence ratio in the range $\varphi = 0.5$–2.0, with a larger difference observed at $\varphi = 0.5$. However, these updates have little effect on the IDTs predictions for the 10/90 NH_3/CH_4 blend. Fig. 10 shows the effect of the newly calculated $\dot{C}H_3 + \dot{N}H_2$ and CH_3NH_2 rate constants on the predictions using the latest Zhang et al. model [8] and the He et al. model [13] from the literature. The new rate constants increase the reactivity for NH_3/CH_4 mixtures both at low- and high-temperatures in the He et al. model. However, there is little difference observed between the updated and original predictions using the Zhang et al. model at these conditions. It should be noted that the rate constants from Dean and Bozzelli [9] and Jodkowski et al. [10] for R1 were used in the Zhang et al. and He et al. models, respectively.

To determine the reasons for the increased NH_3/CH_4 fuel reactivities predicted by our updated model, comparisons of the rate constants and product branching ratios for $\dot{C}H_3 + \dot{N}H_2 \rightleftharpoons$ products before and after these updates are illustrated in Fig. 11. As shown in Fig. 11(a), the Jodkowski rate constant [10] for R1 is ~three times faster than our calculated one at 800 K, while it is up to eight times faster at temperatures above 1800 K. Since R1 is a reactivity-inhibiting reaction pathway for NH_3/CH_4 combustion, this decrease in the R1 rate constant clearly leads to faster IDT predictions. In addition, at 5 atm, the rate constant from Glarborg and Alzueta [12] for R1 is ~40% slower than our calculation at 800 K and ~7.1 times slower at temperatures above 1500 K. At temperatures above 1500 K, it is ~4.5 times slower at 20 atm and ~3.2 times slower at 50 atm. On the other hand, we find the $\dot{C}H_2NH_2 + \dot{H}$ (R2) product channel to be important at high temperatures, in contrast to the previous product branching ratios adopted in the model, which indicated that R2 was negligible, Fig. 11(b). The increased importance of R2 as calculated here, produces more $\dot{H}$ atoms in the radical pool, enhancing chain branching at high temperatures and thus promoting

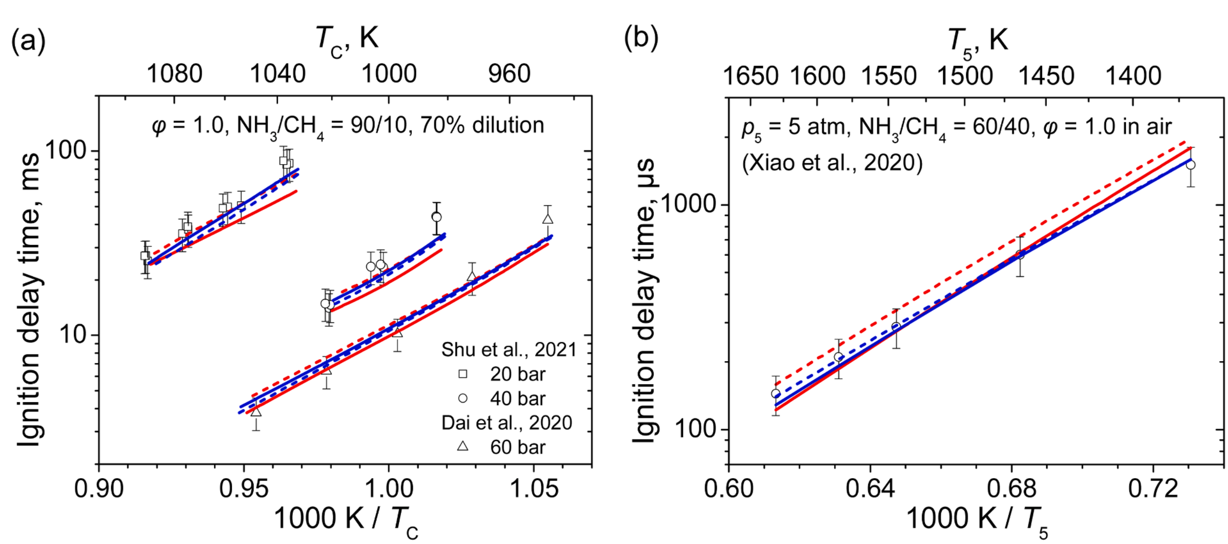

Fig. 10. Effect of the new $\dot{C}H_3 + \dot{N}H_2$ rate constants on predictions using the Zhang et al. model [8] (blue lines) and He et al. model [13] (red lines) for (a) low-temperature and (b) high-temperature IDTs of NH_3/CH_4 mixtures. Symbols: experimental data [6,7,61]. Solid lines: updated model predictions, dashed lines: original model predictions.

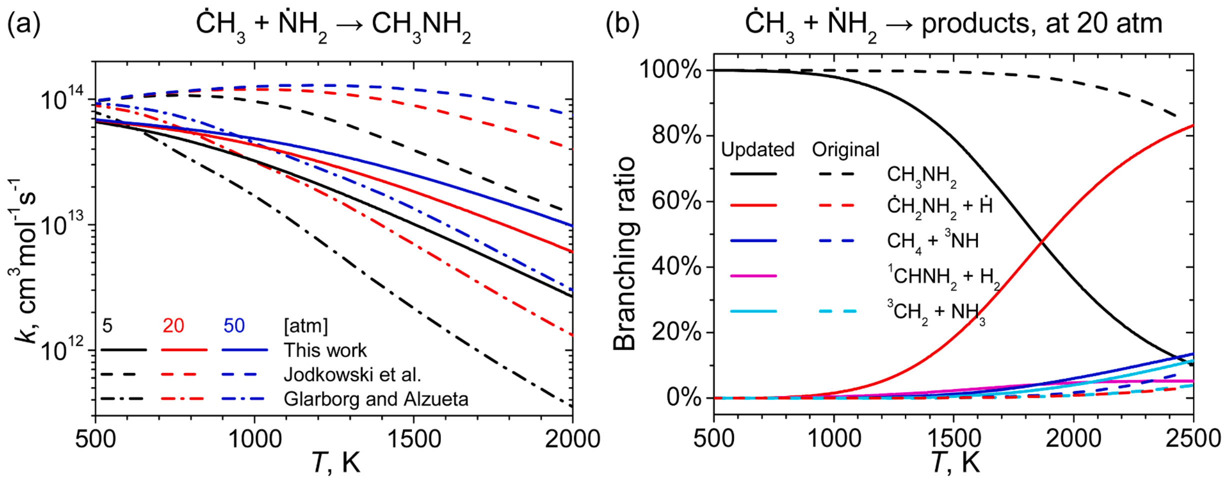

Fig. 11. Comparisons of (a) the rate constants for R1 calculated in this study and those available in the literature [10,12], and (b) the branching ratios for $\dot{C}H_3 + \dot{N}H_2$ = products before and after the kinetic data update (R3 and R7 are negligible in both cases and are not plotted).

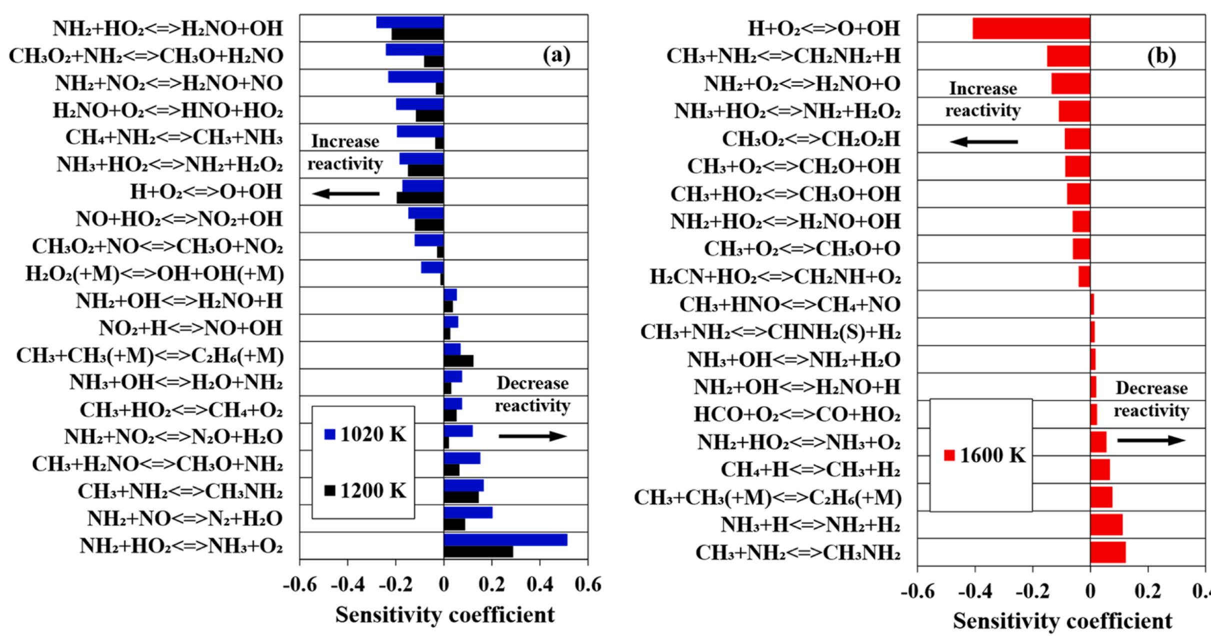

Fig. 12. Brute-force IDT sensitivity analyses for (80/20) NH_3/CH_4 mixture at p = 20 atm, φ = 1.0 at 70 % Ar dilution.

Novelty and significance statement

The reactions of $\dot{C}H_3 + \dot{N}H_2$ have been identified in recent kinetic modeling efforts as key C–N interaction reactions dictating NH_3/CH_4 fuel reactivity. However, the currently available rate constants for $\dot{C}H_3 + \dot{N}H_2$ were determined through extrapolation from limited kinetic measurements or estimations, leading to significant uncertainties. This is the first study to investigate the kinetics of $\dot{C}H_3 + \dot{N}H_2$ using high-level ab initio electronic structure methods and sophisticated kinetic theory, providing more reliable rate expressions for chemical kinetic model development.

fuel reactivity. The other product channels of R3–R7 show little significance in controlling the NH_3/CH_4 fuel reactivity.

In general, the updated kinetic data for $\dot{C}H_3 + \dot{N}H_2$ improves our model predictions for some conditions but leads to slightly poorer predictions for others, particularly in the low-temperature regime. This likely indicates that uncertainties remain in some other important C–N interaction reactions. Sensitivity analyses to IDT have been performed using the updated model, with the important reactions controlling the fuel reactivity of an 80/20 mol % NH_3/CH_4 mixture highlighted in Fig. 12, at temperatures of 1020, 1200 and 1600 K, respectively, at p = 20 atm and φ = 1.0. In addition to the $\dot{C}H_3 + \dot{N}H_2$ reactions studied here, other C–N interaction reactions such as $\dot{C}H_3 + H_2N\dot{O}$ and $CH_3\dot{O}_2 + \dot{N}H_2$ products are also important, particularly at low temperatures. Therefore, further investigations are needed to obtain accurate kinetic predictions for these reactions to improve the model predictions at low-to-intermediate temperatures.

4. Conclusions

The detailed reaction potential energy surface of $\dot{C}H_3 + \dot{N}H_2$ has been explored, using the ANL0F method based on optimized molecular geometries and rovibrational properties obtained at the CCSD(T)-F12/cc-pVTZ-F12 level of theory. The coupled cluster electronic energies for the stationary points investigated here show good convergence in terms of the basis set used. The final ANL0F energies obtained, after including corrections to the CCSD(T)/$CBS_{a'Q,5Z}$ reference energies for higher-order excitations, core-valence, harmonic and anharmonic zero-point energy, and relativistic effects generally agree within 0.1 kcal mol^{-1} with ATcT values for stable products. The calculated $\Delta H_{f,0\ K}$ for CH_3NH_2, $\dot{C}H_2NH_2$, $CH_3\dot{N}H$ and $^1CHNH_2$ based on ANL0F energies show a similar level of agreement compared to ATcT values.

VRC-TST calculations were performed to obtain the minimum transitional mode number of states for the barrierless reactions in R1–R3. The interaction energies were directly sampled at the CASPT2-F12 (2e,2o)/cc-pVTZ-F12 level of theory, with one-dimensional energy corrections for geometry relaxation and basis set considered. An RRKM/ME calculation was performed to determine the temperature- and pressure-dependent rate constants and product branching ratios for $\dot{C}H_3 + \dot{N}H_2 \rightleftharpoons$ products. Our calculated rate constants for R1, R–1 and R–4 are in good agreement with available kinetic experimental measurements in the literature. At $T \leq 1400$ K, the formation of CH_3NH_2 (R1) is dominant for pressures in the range of 1–100 atm. At 1500 K, the formation of $\dot{C}H_2NH_2 + \dot{H}$ (R2) starts to compete with R1 and dominates at $T > 2000$ K. The other product channels are generally less significant compared to R1 and R2 over the entire temperature and pressure ranges.

The calculated rate constants for $\dot{C}H_3 + \dot{N}H_2 \rightleftharpoons$ products and $CH_3NH_2 \rightleftharpoons$ products have been incorporated into a NH_3/CH_4 kinetic model under development at Galway. These updates lead to shorter IDT predictions for NH_3/CH_4 combustion in both the low- and high-temperature regimes. This is primarily because the previously adopted rate constant for the reactivity-inhibiting reaction (R1) is significantly faster than our calculation. In addition, our results indicate that R2 is an important product channel at high temperatures but was significantly underestimated in previous studies. Although the updated model performs better compared to shock tube and RCM experimental data from the literature at some conditions, poorer predictions are observed for others, especially in the low-temperature regime. This highlights the need for further investigation of the other important C–N interaction reactions to obtain accurate rate parameters.

CRediT authorship contribution statement

Yuxiang Zhu: Writing – original draft, Investigation. **Stephen J. Klippenstein:** Writing – review & editing, Methodology. **Henry J. Curran:** Writing – review & editing, Supervision. **Chong-Wen Zhou:** Writing – review & editing, Supervision.

Declaration of competing interests

The authors declare that they have no known competing financial interests or personal relationships that could have appeared to influence the work reported in this paper.

Acknowledgements

The authors acknowledge computational resources provided by the Irish Centre for High-End Computing (ICHEC) under project number ‘p200362’. Work at Argonne National Laboratory was supported by the US Department of Energy, Office of Science, Basic Energy Sciences, Division of Chemical Sciences, Geosciences, and Biosciences under contract No. DE-AC02–06CH11357.

Supplementary materials

Supplementary material associated with this article can be found, in the online version, at doi:10.1016/j.combustflame.2025.114232.

References

[1] N. Gray, S. McDonagh, R. O'Shea, B. Smyth, J.D. Murphy, Decarbonising ships, planes and trucks: an analysis of suitable low-carbon fuels for the maritime, aviation and haulage sectors, Adv. Appl. Energy 1 (2021) 100008.
[2] A. Valera-Medina, F. Amer-Hatem, A. Azad, I. Dedoussi, M. De Joannon, R. Fernandes, P. Glarborg, H. Hashemi, X. He, S. Mashruk, Review on ammonia as a potential fuel: from synthesis to economics, Energy Fuels. 35 (2021) 6964–7029.
[3] H. Kobayashi, A. Hayakawa, K.K.A. Somarathne, E.C. Okafor, Science and technology of ammonia combustion, Proc. Combust. Inst. 37 (2019) 109–133.
[4] A. Valera-Medina, R. Marsh, J. Runyon, D. Pugh, P. Beasley, T. Hughes, P. Bowen, Ammonia–methane combustion in tangential swirl burners for gas turbine power generation, Appl. Energy 185 (2017) 1362–1371.
[5] P. Glarborg, J.A. Miller, B. Ruscic, S.J. Klippenstein, Modeling nitrogen chemistry in combustion, Prog. Energy Combust. Sci. 67 (2018) 31–68.
[6] L. Dai, S. Gersen, P. Glarborg, A. Mokhov, H. Levinsky, Autoignition studies of NH_3/CH_4 mixtures at high pressure, Combust. Flame 218 (2020) 19–26.
[7] B. Shu, X. He, C. Ramos, R. Fernandes, M. Costa, Experimental and modeling study on the auto-ignition properties of ammonia/methane mixtures at elevated pressures, Proc. Combust. Inst. 38 (2021) 261–268.
[8] X. Zhang, K.K. Yalamanchi, S.M. Sarathy, Combustion chemistry of ammonia/C_1 fuels: a comprehensive kinetic modeling study, Fuel 341 (2023) 127676.
[9] A.M. Dean, J.W. Bozzelli, Combustion chemistry of nitrogen, Gas-phase combustion chemistry, (2000) 125–341.
[10] J.T. Jodkowski, E. Ratajczak, K. Fagerström, A. Lund, N.D. Stothard, R. Humpfer, H.-H. Grotheer, Kinetics of the cross reaction between amidogen and methyl radicals, Chem. Phys. Lett. 240 (1995) 63–71.
[11] M. Votsmeier, S. Song, D. Davidson, R. Hanson, Shock tube study of monomethylamine thermal decomposition and NH_2 high temperature absorption coefficient, Int. J. Chem. Kinet. 31 (1999) 323–330.
[12] P. Glarborg, M.U. Alzueta, Decomposition of CH_3NH_2: implications for CH_X/NH_y radical–radical reactions, Int. J. Chem. Kinet. 57 (2025) 77–90.
[13] X. He, M. Li, B. Shu, R. Fernandes, K. Moshammer, Exploring the effect of different reactivity promoters on the oxidation of ammonia in a jet-stirred reactor, J. Phys. Chem. A 127 (2023) 1923–1940.
[14] P. Glarborg, C.S. Andreasen, H. Hashemi, R. Qian, P. Marshall, Oxidation of methylamine, Int. J. Chem. Kinet. 52 (2020) 893–906.
[15] L. Dai, H. Hashemi, P. Glarborg, S. Gersen, P. Marshall, A. Mokhov, H. Levinsky, Ignition delay times of NH3/DME blends at high pressure and low DME fraction: RCM experiments and simulations, Combust. Flame 227 (2021) 120–134.
[16] M. Quack, J. Troe, Unimolecular processes V: maximum free energy criterion for the high pressure limit of dissociation reactions, Ber. Bunsenges. Phys. Chem. 81 (1977) 329–337.
[17] R. Gilbert, K. Luther, J. Troe, Theory of thermal unimolecular reactions in the fall-off range. II. Weak collision rate constants, Ber. Bunsenges. Phys. Chem. 87 (1983) 169–177.
[18] S.J. Klippenstein, P. Glarborg, Theoretical kinetics predictions for $NH_2 + HO_2$, Combust. Flame 236 (2022) 111787.
[19] S.J. Klippenstein, L.B. Harding, B. Ruscic, Ab initio computations and active thermochemical tables hand in hand: heats of formation of core combustion species, J. Phys. Chem. A 121 (2017) 6580–6602.
[20] G. Knizia, T.B. Adler, H.-J. Werner, Simplified CCSD (T)-F12 methods: theory and benchmarks, J. Chem. Phys. 130 (2009) 054104.
[21] K.A. Peterson, T.B. Adler, H.-J. Werner, Systematically convergent basis sets for explicitly correlated wavefunctions: the atoms H, He, B–Ne, and Al–Ar, J. Chem. Phys. 128 (2008) 084102.
[22] S. Grimme, J. Antony, S. Ehrlich, H. Krieg, A consistent and accurate ab initio parametrization of density functional dispersion correction (DFT-D) for the 94 elements H-Pu, J. Chem. Phys. 132 (2010) 154104.
[23] T.H. Dunning Jr, Gaussian basis sets for use in correlated molecular calculations. I. The atoms boron through neon and hydrogen, J. Chem. Phys. 90 (1989) 1007–1023.
[24] J.D. Watts, J. Gauss, R.J. Bartlett, Coupled-cluster methods with noniterative triple excitations for restricted open-shell Hartree–Fock and other general single determinant reference functions. Energies and analytical gradients, J. Chem. Phys. 98 (1993) 8718–8733.
[25] D.E. Woon, T.H. Dunning Jr, Gaussian basis sets for use in correlated molecular calculations. V. Core-valence basis sets for boron through neon, J. Chem. Phys. 103 (1995) 4572–4585.
[26] Y.J. Bomble, J.F. Stanton, M. Kállay, J. Gauss, Coupled-cluster methods including noniterative corrections for quadruple excitations, J. Chem. Phys. 123 (2005) 054101.
[27] J. Bloino, M. Biczysko, V. Barone, General perturbative approach for spectroscopy, thermodynamics, and kinetics: methodological background and benchmark studies, J. Chem. Theory. Comput. 8 (2012) 1015–1036.

[28] D. Peng, M. Reiher, Exact decoupling of the relativistic fock operator, Theor. Chem. Acc. 131 (2012) 1–20.
[29] H.-J. Werner, P.J. Knowles, R. Lindh, et al., MOLPRO, A Package of Ab Initio Programs, 2015.
[30] MRCC, A string-based quantum chemical program suite; written by M. Kállay, see also M.; Kállay, P.R. Surján, higher excitations in coupled-cluster theory, J. Chem. Phys. 115 (2001) 945–2954.
[31] Gaussian 09, M.J. Frisch, G.W. Trucks, H.B. Schlegel, et al., Gaussian, Inc., Wallingford CT, 2009.
[32] S.J. Klippenstein, From theoretical reaction dynamics to chemical modeling of combustion, Proc. Combust. Inst. 36 (2017) 77–111.
[33] L.B. Harding, Y. Georgievskii, S.J. Klippenstein, Predictive theory for hydrogen atom− hydrocarbon radical association kinetics, J. Phys. Chem. A 109 (2005) 4646–4656.
[34] Y. Georgievskii, S.J. Klippenstein, Transition state theory for multichannel addition reactions: multifaceted dividing surfaces, J. Phys. Chem. A 107 (2003) 9776–9781.
[35] Y. Georgievskii, S.J. Klippenstein, Variable reaction coordinate transition state theory: analytic results and application to the $C_2H_3 + H \rightarrow C_2H_4$ reaction, J. Chem. Phys. 118 (2003) 5442–5455.
[36] S.J. Klippenstein, Variational optimizations in the Rice–Ramsperger–Kassel–Marcus theory calculations for unimolecular dissociations with no reverse barrier, J. Chem. Phys. 96 (1992) 367–371.
[37] Y. Georgievskii, L.B. Harding, S.J. Klippenstein, VaReCoF, Argonne National Laboratory, 2016, 3.23.
[38] S.J. Klippenstein, Y. Georgievskii, L.B. Harding, Predictive theory for the combination kinetics of two alkyl radicals, Phys. Chem. Chem. Phys. 8 (2006) 1133–1147.
[39] S.J. Klippenstein, W.D. Allen, Variable reaction coordinate direct RRKM theory, Ber. Bunsenges. Phys. Chem. 101 (1997) 423–437.
[40] T. Shiozaki, H.-J. Werner, Communication: second-order multireference perturbation theory with explicit correlation: CASPT2-F12, J. Chem. Phys. 133 (2010) 141103.
[41] T. Shiozaki, G. Knizia, H.-J. Werner, Explicitly correlated multireference configuration interaction: MRCI-F12, J. Chem. Phys. 134 (2011) 034113.
[42] T. Shiozaki, H.-J. Werner, Explicitly correlated multireference configuration interaction with multiple reference functions: avoided crossings and conical intersections, J. Chem. Phys. 134 (2011) 184104.
[43] T. Shiozaki, H.-J. Werner, Multireference explicitly correlated F12 theories, Mol. Phys. 111 (2013) 607–630.
[44] G. Ghigo, B.O. Roos, P.-Å. Malmqvist, A modified definition of the zeroth-order Hamiltonian in multiconfigurational perturbation theory (CASPT2), Chem. Phys. Lett. 396 (2004) 142–149.
[45] M.G. Evans, P. M, Some applications of the transition state method to the calculation of reaction velocities, especially in solution, Trans. Faraday Soc. 31 (1935) 875.
[46] H. Eyring, The activated complex in chemical reactions, J. Chem. Phys. 3 (1935) 107–115.
[47] C. Eckart, The penetration of a potential barrier by electrons, Phys. Rev. 35 (1930) 1303.
[48] M.S. Johnson, X. Dong, A. Grinberg Dana, Y. Chung, D. Farina Jr, R.J. Gillis, M. Liu, N.W. Yee, K. Blondal, E. Mazeau, RMG database for chemical property prediction, J. Chem. Inf. Model. 62 (2022) 4906–4915.
[49] Y. Georgievskii, J.A. Miller, M.P. Burke, S.J. Klippenstein, Reformulation and solution of the master equation for multiple-well chemical reactions, J. Phys. Chem. A 117 (2013) 12146–12154.
[50] https://github.com/Auto-Mech/MESS [accessed 2024.05].
[51] B. Ruscic, D.H. Bross, Active Thermochemical Tables (ATcT) values based on ver. 1.130 of the Thermochemical Network, Argonne National Laboratory, Lemont, Illinois, 2023, https://doi.org/10.17038/CSE/1997229 available at ATcT.anl.gov.
[52] S.N. Elliott, M. Keçeli, M.K. Ghosh, K.P. Somers, H.J. Curran, S.J. Klippenstein, High-accuracy heats of formation for alkane oxidation: from small to large via the automated CBH-anl method, J. Phys. Chem. A 127 (2023) 1512–1531.
[53] M. Keçeli, S.N. Elliott, Y.-P. Li, M.S. Johnson, C. Cavallotti, Y. Georgievskii, W. H. Green, M. Pelucchi, J.M. Wozniak, A.W. Jasper, Automated computational thermochemistry for butane oxidation: a prelude to predictive automated combustion kinetics, Proc. Combust. Inst. 37 (2019) 363–371.
[54] B.J. McBride, Computer program for calculating and fitting thermodynamic functions, 1271 (1992).
[55] M. Röhrig, H.G. Wagner, A kinetic study about the reactions of NH ($X^3\Sigma^-$) with hydrocarbons part 1: saturated hydrocarbons and acetaldehyde, Ber. Bunsenges. Phys. Chem. 98 (1994) 858–863.
[56] B. Wang, H. Hou, Y. Gu, Ab initio and kinetic calculations for the reactions of NH ($X^3\Sigma^-$) with CH_xF_{4-x} and CD_xF_{4-x} (x = 1, 2, 3, 4), J. Phys. Chem. A 103 (1999) 9049–9054.
[57] Z.-F. Xu, S.-M. Li, Y.-X. Yu, Z.-S. Li, C.-C. Sun, Theoretical studies on the reaction path dynamics and variational transition-state theory rate constants of the hydrogen-abstraction reactions of the NH ($X^3\Sigma^-$) radical with methane and ethane, J. Phys. Chem. A 103 (1999) 4910–4917.
[58] J. Bugler, K.P. Somers, J.M. Simmie, F. Guthe, H.J. Curran, Modeling nitrogen species as pollutants: thermochemical influences, J. Phys. Chem. A 120 (2016) 7192–7197.
[59] Y. Zhu, H.J. Curran, S. Girhe, Y. Murakami, H. Pitsch, K. Senecal, L. Yang, C.-W. Zhou, The combustion chemistry of ammonia and ammonia/hydrogen mixtures: a comprehensive chemical kinetic modeling study, Combust. Flame 260 (2024) 113239.
[60] P. Wang, J. Caravaca-Vilchez, T. Nagy, S. Dong, X. Cheng, K.A. Heufer, H. J. Curran, A focus on the first-stage ignition of *n*-pentane, Combust. Flame (2024) preparing for submission.
[61] H. Xiao, S. Lai, A. Valera-Medina, J. Li, J. Liu, H. Fu, Experimental and modeling study on ignition delay of ammonia/methane fuels, Int. J. Energy Res. 44 (2020) 6939–6949.
[62] H. Xiao, A. Chen, Y. Guo, L. Zhang, M. Zhang, X. Deng, J. Li, W. Ying, Auto-ignition delay characteristics of ammonia substitution on methane, Processes 10 (2022) 2214.
[63] D.G. Goodwin, H.K. Moffat, I. Schoegl, et al., Cantera: an object-oriented software toolkit for chemical kinetics, thermodynamics, and transport processes. https://www.cantera.org, 2022. Version 2.6.0. doi:10.5281/zenodo.6387882.